Front. Energy 2023, 17(4): 555–566
https://doi.org/10.1007/s11708-023-0882-8

RESEARCH ARTICLE

Shixian XIONG, Hongcheng KE, Lei CAO, Yu WANG, Qian ZHU, Liqin ZHONG, Lanlan FAN, Feng GU

CC@BCN@PANI core-shell nanoarrays as ultra-high cycle stability cathode for Zn-ion hybrid supercapacitors

Abstract Exploring cathode materials that combine excellent cycling stability and high energy density poses a challenge to aqueous Zn-ion hybrid supercapacitors (ZHSCs). Herein, polyaniline (PANI) coated boron-carbon-nitrogen (BCN) nanoarray on carbon cloth surface is prepared as advanced cathode materials via simple high-temperature calcination and electrochemical deposition methods. Because of the excellent specific capacity and conductivity of PANI, the CC@BCN@PANI core-shell nanoarrays cathode shows an excellent ion storage capability. Moreover, the 3D nanoarray structure can provide enough space for the volume expansion and contraction of PANI in the charging/discharging cycles, which effectively avoids the collapse of the microstructure and greatly improves the electrochemical stability of PANI. Therefore, the CC@BCN@PANI-based ZHSCs exhibit superior electrochemical performances showing a specific capacity of 145.8 mAh/g, a high energy density of 116.78 Wh/kg, an excellent power density of 12 kW/kg, and a capacity retention rate of 86.2% after 8000 charge/discharge cycles at a current density of 2 A/g. In addition, the flexible ZHSCs (FZHSCs) also show a capacity retention rate of 87.7% at the current density of 2 A/g after 450 cycles.

Keywords CC@BCN@PANI cathode, Zn-ion hybrid supercapacitor, core-shell nanoarrays, high energy density, ultra-high cycle stability

Received Feb. 18, 2023; accepted May 6, 2023; online Jun. 20, 2023

Shixian XIONG, Hongcheng KE, Lei CAO (✉), Yu WANG, Qian ZHU, Liqin ZHONG, Lanlan FAN (✉), Feng GU (✉)
Nanchang Key Laboratory for Advanced Manufacturing of Electronic Information Materials and Devices/Jiangxi Provincial Key Laboratory for Simulation and Modelling of Particulate Systems, International Institute for Innovation, Jiangxi University of Science and Technology, Nanchang 330013, China
E-mails: lei.cao@jxust.edu.cn (L. CAO); llfan@jxust.edu.cn (L. FAN); feng.gu@jxust.edu.cn (F. GU)

1 Introduction

With the growing need for foldable and wearable electronic devices, researchers are concentrating on creating electrochemical energy storage (EES) systems that can provide rapid charging and discharging capabilities, high energy density, and improved security features [1–4]. Supercapacitors (SCs) were initially considered for this purpose due to their high-power density, fast charging speed, and excellent cycling stability [5]. However, compared with rechargeable batteries, the low energy density limits its further development [6–8]. Hence, the promising strategy for augmenting the energy density of EES systems is the fabrication of hybrid supercapacitors (HSCs), which combine the advantages of rechargeable batteries and SCs [9].

Due to the scarcity and high reactivity [10,11], alkali metal resources such as Li, Na, and K used in single-valent HSCs cannot be used together with aqueous electrolytes, while most organic electrolytes are toxic and prone to explosion [12]. Compared with single-valent metal ion HSCs, divalent metal ion HSCs (such as Zn^{2+}, Mg^{2+}, and Ca^{2+}) have the advantages of low cost, large capacity, safety, and no pollution [13–15]. From many divalent HSCs, Zn-ion hybrid supercapacitors (ZHSCs) stand out because of the abundant Zn resources with high theoretical capacity (820 mAh/g), lower redox potential (−0.76 V versus standard hydrogen electrode), low cost and high safety [16–18]. In addition, flexible ZHSCs (FZHSCs) have also attracted widespread attention from researchers due to their ease of integration, high flexibility, high safety, and wearability. However, recent studies have found that the active material used in the flexible electrode of FZHSCs is prone to detachment and fracture during the bending process, resulting in a gradual decrease in energy density and rapid degradation of cycle life. Therefore, the new flexible composite material needs to be developed to improve its electrochemical performance [19]. For example, Pu et al. succeeded in synthesizing the 3D nitrogen-doped carbon nanotube

array fiber electrode. This 3D nanoarray structure exhibits an excellent stress release ability during continuous electrode bending, avoiding the shedding of the active material and maintaining an excellent electrochemical stability [20]. However, its ion adsorption and desorption energy storage mechanism, which is still mainly based on the double-layer capacitance, limits the further increase of energy density of FZHSCs. Therefore, the pseudocapacitive materials with high specific capacity need to be introduced to improve this defect.

Typical conductive polymers, such as polypyrrole and polyaniline (PANI), are considered a charming pseudocapacitive material for ZHSCs which had a great potential on account of its excellent exceptional electrical conductivity, simple synthesis, and incredibly high ion storing capacity [21,22]. Moreover, PANI exhibits dissimilar properties compared to vanadium oxides and manganese oxides, whose inherent flexibility allows for its utilization in the construction of cathodes for FZHSCs. But the unsatisfactory rate performance and limited cycle life of PANI-based ZHSCs have hindered their advancement [23,24]. Compared with PANI, carbon-based materials are widely studied for their excellent electrical conductivity and chemical stability [5,11,25]. Unfortunately, the energy storage mechanism of the double-layer capacitor result in a low ion storage capacity, which limits the improvement of energy density. Therefore, combining PANI with carbon materials that possess a high electrical conductivity and a chemical stability appears to be a feasible approach. Recent studies have shown that doping of B and N atoms in the framework of carbon materials (BCN) can transform the electrochemical negativity of C atoms, and activate the the electron activity, which in turn improves the stability and energy density of electrode materials [26–29]. Furthermore, BCN materials can be fabricated into BCN nanotube arrays using specific processing techniques, which can enhance the intermolecular interaction between the substrate material and PANI and improve its structural stability [30,31]. Therefore, it is of significant importance to advance the development of high-performance ZHSCs by utilizing low-cost and abundant raw materials and obtaining a positive electrode material with excellent capacitance performance through a simple and secure synthetic method.

Herein, PANI-coated BCN core-shell nanoarrays were constructed on the surface of carbon cloth (CC@BCN@PANI) by utilizing the simple calcination and electrochemical deposition method. First, the 3D nanoarray structure of CC@BCN@PANI could release the stresses to maintain a structural stability under twisting conditions. In addition, this structure can also provide space for the expansion and contraction of PANI molecular chains during the charging and discharging process. Besides, PANI coating on the BCN nanoarray surface can greatly increase its contact area with the electrolyte, facilitating the adsorption and infiltration of the ions. To demonstrate the excellent electrochemical performance of CC@BCN@PANI, the obtained CC@BCN@PANI//Zn exhibite a significantly enhanced rate capability, a high specific capacitance of 145.8 mAh/g (at the current density of 0.5 A/g), a high energy density of 116.78 Wh/kg, and an excellent power density of 12 kW/kg. Moreover, the ZHSCs show a fast charge/discharge capability and a long cycle stability (86% capacity remaining after 8000 charge/discharge cycles at a current density of 2 A/g, and the Coulombic efficiency close to 100%). Furthermore, the flexible quasi-solid-state ZHSCs fabricated by CC@BCN@PANI cathodes show a high reversible discharge capacity of 160 mAh/g at the current density of 0.1 A/g. This research will provide new methods and knowledge for the development of new high-performance flexible electrodes.

2 Experiment

2.1 Preparation of CC@BCN

First, wash the carbon cloth (CC) (Hesem, Shanghai) with deionized water and anhydrous alcohol and dry. Then dissolve 10 g urea (CH_4N_2O) (Macklin, AR), 1 g polyethylene glycol (PEG-2000, Macklin, AR), and 0.3 g boric acid (H_3BO_3) into 100 mL deionized (DI) water. Afterwards, immerse the CC in the above solution and dry in an oven at 100 °C for 10 h. Finally, the precursor was calcined at a high temperature (900 °C) for 4 h under a nitrogen atmosphere. Now the CC@BCN nanoarrays electrode was generated. The mass of BCN nanoarrays loading is about 1.2–1.6 mg/cm^2.

2.2 Preparation of CC@BCN@PANI and CC@PANI

The CC@BCN@PANI nanoarrays were produced by electrodeposition in an electro-deposition solution comprising 2.5 g of aniline (Macklin, AR), 5.4 mL of H_2SO_4 (Xilong Scientific, AR), 14.2 g of Na_2SO_4 (Xilong Scientific, AR), and 200 mL of DI water. The obtained CC@BCN nanoarrays electrode as the working electrode, the Pt sheet as the counter electrode, and a standard calomel electrode (SCE) served as the reference electrode. Electrodeposition was carried in a voltage range of −0.2 to 1 V and a current sweep speed of 50 mV/s for 16 cycles. Then, under the same conditions, the CC@PANI electrode was obtained with a CC substrate as the working electrode under the same electrodeposition conditions. To clean the residual electrodeposition solution on the surface, the gained electrodes were washed with DI water 3 times and dried under vacuum at 60° for 3 h. The mass of PANI on the electrode was approximately 0.8–1.2 mg/cm^2.

2.3 Preparation of $ZnSO_4$/gelatin gel electrolyte (GGE)

4 g of gelatin (Macklin, AR) was dispersed in 40 mL of 1 mol/L $ZnSO_4$ aqueous solution under stirring at 60 °C. Then for cross-linking, a certain volume of glutaraldehyde solution was applied.

2.4 Assembly of coin-type ZHSCs and sandwich-type FZHSCs

To assess the electrochemical characteristics of the materials, the CC@BCN, CC@PANI, and CC@BCN@PANI electrodes were used as cathodes, commercial Zn plates as anode electrodes, 1 mol/L of $ZnSO_4$ aqueous solution as electrolyte, and fiberglass as the separator to assemble coin-type CR2032 ZHSCs.

Sandwich-type FZHSCs devices were also fabricated. To be specific, the nanocomposite CC@BCN@PANI (1 cm × 3.5 cm) cathodes and commercial Zn foil (30 μm in thickness, 1 cm × 3.5 cm) anodes were used as cathodes and anodes, which were separated by GGE, and polyimide tape was used for encapsulation at last.

2.5 Material characterization

Scanning electron microscopy (SEM, type specification: ZEISS 300) was used to measure the surface microstructure of the three cathodes. X-ray diffraction (XRD, 5°–90°, 10°/min, model: D8 advance, US) was used to measure the composition and crystal structure. X-ray photoelectron spectroscopy (XPS, type specification: ESCALAB 250) was used to detect the chemical bonds. Fourier-transform infrared (FTIR) spectroscope (GREAT 20, RuiJ) was used to measure the chemical bond and molecular structure.

2.6 Electrochemical measurements

Cyclic voltammetry (CV), galvanostatic charge-discharge (GCD) and electrochemical impedance spectroscopy (EIS) were tested in the CHI 660E (Chenhua Instrument, Shanghai). The rate and cycling stability performance of ZHSCs and flexible devices were measured by a Neware BTS8000 battery testing system. The EIS was tested at open circuit voltage, whose frequency ranges from 10 mHz to 100 kHz and AC amplitude is 5 mV. The CV performances of ZHSCs and FZHSCs were measured at the voltage range of 0.1–1.6 V. The current densities of GCD measurements were in the range of 0.5–15 A/g (ZHSCs), and 0.1–2 A/g (FZHSCs).

The gravimetric specific capacity (C_m, mAh/g) is calculated based on the GCD curves by

$$C_m = \frac{I\Delta t}{3.6m}, \tag{1}$$

$$E = \frac{1}{2} \times C_m \times \Delta V, \tag{2}$$

$$P = \frac{E}{t} \times 3600, \tag{3}$$

where I is the current (A), Δt is the discharging time (s), ΔV is the potential window (V), m is the mass of active materials (g), E is the energy density (Wh/kg), and P is the power density (W/kg).

3 Results and discussion

The typical preparation of the CC@BCN@PANI cathode is shown in Fig. 1. Initially, the CC was put into a precursor solution of BCN comprising PEG-2000, CH_4N_2O, and H_3BO_3 for 5 h, and the mixture was subsequently dried at 100 °C for 4 h in an oven to promote pre-crosslinking of the reactants into BCN precursors. Subsequently, the CC@BCN precursors were calcined at 900 °C for 4 h in the tube furnace to prepare CC@BCN 3D nanoarrays. PANI was then electrochemi-

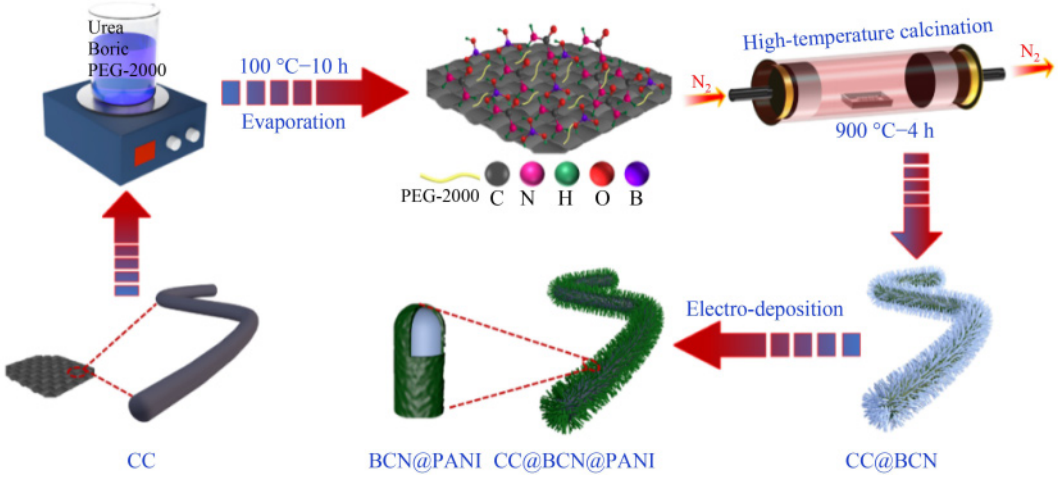

Fig. 1 Synthetic illustration of CC@BCN@PANI cathode.

cally deposited on the surface of the CC@BCN 3D nanoarrays to obtain CC@BCN@PANI. The possible formation mechanism of BCN nanoarrays could be attributed to the B, N, and C atoms, forming a nanosheet structure comparable to the graphene network at a certain temperature. Then, the BCN nanosheet gradually extruded and rolled into BCN 3D nanoarrays with the temperature increase [32,33].

The morphology of electrode materials was examined by SEM. Compared to the smooth surface of CC (Fig. S1(a) in the Electronic Supplementary Material (ESM)), the surface of CC@BCN (Figs. 2(a) and 2(b)) is uniformly grown with 3D nanoarrays of BCN, which can increase the contact area with the electrolyte. Moreover, the 3D nanoarray structure could prevent breaking and falling off of the active material during bending and endure the volume expansion/contraction phenomenon of PANI [34,35]. Compared with the CC@BCN, the BCN nanoarrays of CC@BCN@PANI were completely coated by a layer of rough PANI (Figs. 2(c) and 2(d)), confirming the formation of a core-shell flexible electrode material. This structure gave full play to the advantage of the high electrical conductivity and fast ion transport capability of BCN nanoarrays, as well as the high specific capacitance of the PANI shell. Figures S1(b) and S1(c) in the ESM show the images of CC@PANI. It can be seen that irregular PANI was unevenly distributed on the surface of CC, which is caused by poor infiltration of CC and electrolyte. As displayed in Figs. 2(e) and 2(f), the elemental mapping images confirmed that B, C, N, and S were homogeneously distributed at CC@BCN@PANI electrodes. The presence of S was attributed to the sulfate ions in the electrodeposition solution adsorbed by CC and CC@BCN during the electrodeposition process of PANI.

XRD testing was used to analyze the crystal structure of electrode materials. As shown in Fig. 3(a), two broad characteristic peaks of the electrode materials were detected around 25.3° and 43°, indicating the (002) and (100) crystal planes of carbon material, which were similar to the XRD spectrum of BCN materials reported earlier [32,36]. To demonstrate that the surface of CC was successful *in situ* growth of BCN nanoarrays, and the deposition of PANI on CC@BCN, FTIR spectroscopy was used to assess the vibration patterns of specific chemical groups (Fig. 3(b)). The inconspicuous peak nearby 3729 cm^{-1} was put down to the stretching vibration of N–H bonds. Besides, two same absorption bands of CC@BCN at 1381 cm^{-1} and 835 cm^{-1} were applied to the intimal tensile vibration and outer bond bending vibrations of B–N [37,38]. The peaks of C=C stretching vibration were observed near 1573 cm^{-1}, and a peak of 696 cm^{-1} was applied to B–C bonds. Furthermore, the characteristic peaks of CC@BCN located at 1196 cm^{-1} and 1689 cm^{-1} were applied to the stretching vibrations of C=N and C–N. The spectrum of CC@BCN@PANI samples was similar to that of the CC@PANI. This was attributed to the uniform deposition of PANI on the surface of CC@BCN nanoarrays and the weak depth of infrared light absorption into the sample layer to detect the CC@BCN characteristic peak. Moreover, the peaks situated at 1557 cm^{-1} and 1473 cm^{-1} were consistent with the characteristic peaks of the stretching vibration of quinoid and benzenoid rings, and the vibration and stretching of the characteristic peaks at the peaks 1300 cm^{-1} corresponded to the C=N bonds [39]. The peaks at 1117 cm^{-1} and 798 cm^{-1} were consistent with the C–H stretching vibration in quinoid and benzenoid rings.

XPS was used for analyzing the element type and valence bond composition of electrode materials. Figure 3(c)

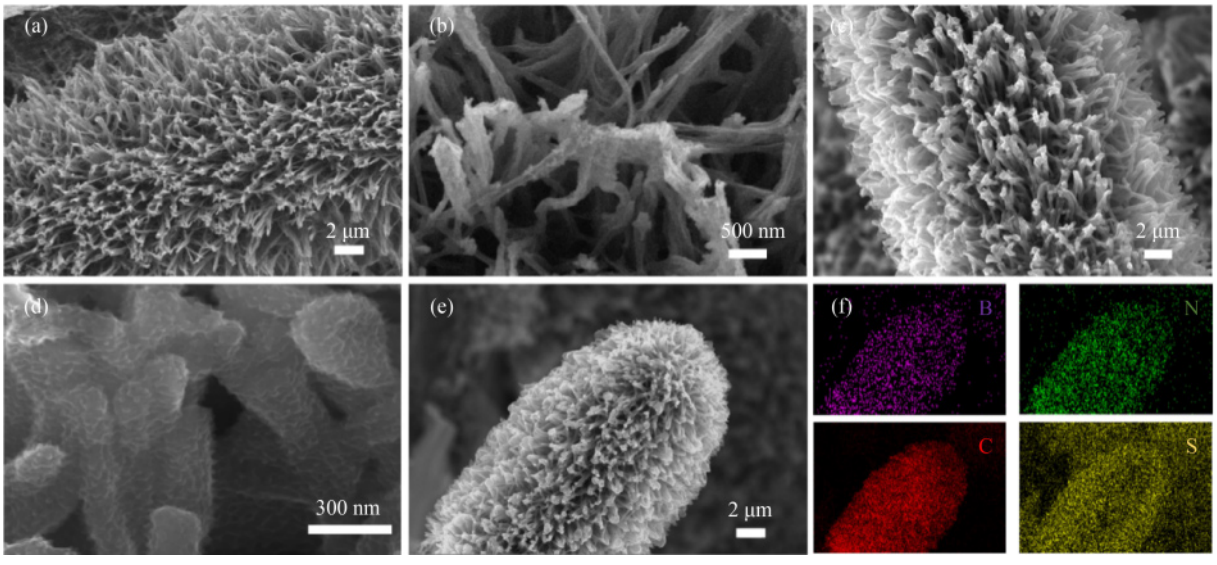

Fig. 2 SEM characterization of electrode materials.
(a, b) CC@BCN; (c–e) CC@BCN@PANI; (f) elemental mapping images of CC@BCN@PANI.

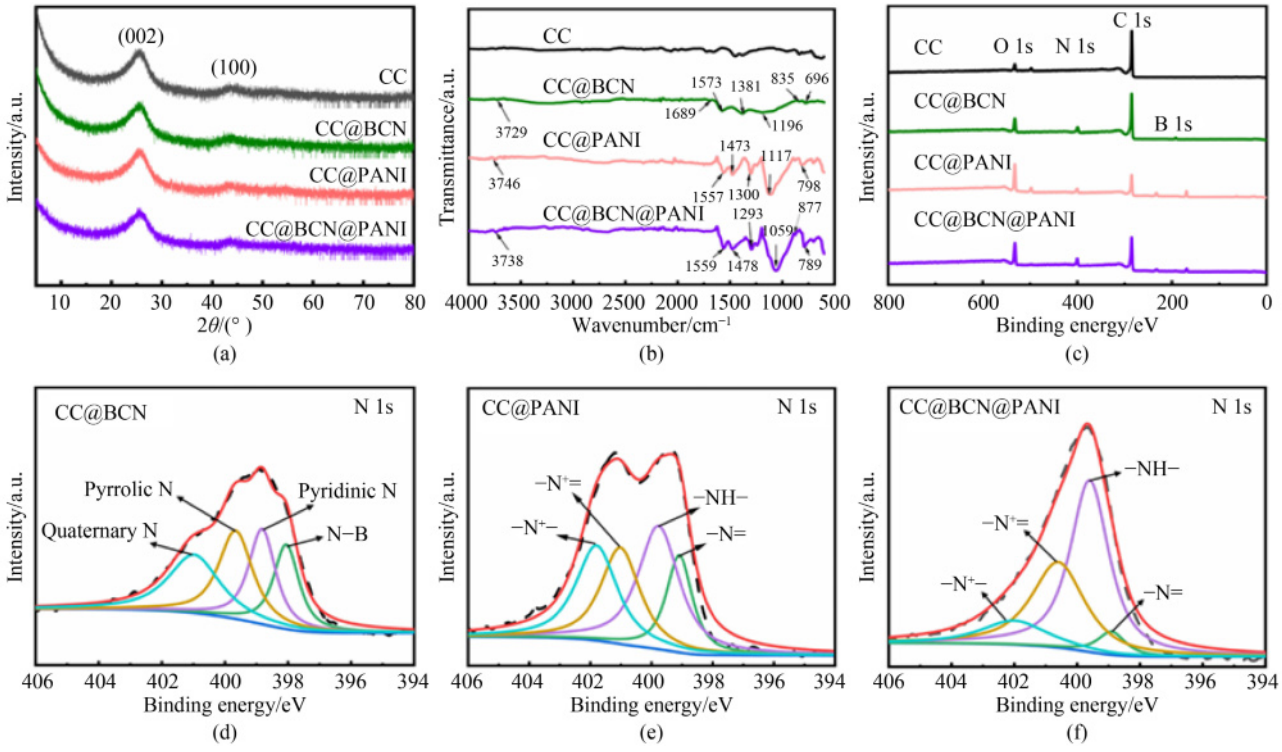

Fig. 3 Characterization of electrode materials.

(a) XRD patterns; (b) FTIR spectra and (c) XPS spectra of CC, CC@BCN, CC@PANI, and CC@BCN@PANI; (d) XPS spectra N 1s of CC@BCN; (e) XPS spectra N 1s of CC@PANI; (f) XPS spectra N 1s of CC@BCN@PANI.

exhibited the full survey spectra of electrode materials, in which the B 1s, C 1s, N 1s, and O 1s sharp peaks were observed at 192.08, 285.08, 400.08, and 532.08 eV, respectively. Noticeably, the O 1s peaks were significantly stronger in CC@BCN, CC@PANI, and CC@BCN@PANI samples compared with the CC, which could increase the wettability of electrolyte and improve Zn^{2+} chemical adsorption [40]. B 1s and N 1s peaks in CC@BCN samples meant that BCN nanoarrays were successfully grown on the CC surface. In particular, the electron could be repositioned and activated by the B atom as a recipient and the N atom as a provider of electronic coordination [41].

In Figs. 3(e) and 3(f), the high-resolution XPS N 1s spectrum of CC@PANI and CC@BCN@PANI in Figs. 3(e) and 3(f) were divided into four subpeaks, corresponding to –N= (398.9 eV), –NH– (399.6 eV), $–N^+=$ (400.6 eV), and $–N^+–$ (402 eV), respectively [42]. By contrast, the CC@BCN samples (Fig. 3(d)) were divided into another four peaks: 398, 398.8, 399.6, and 400.1 eV, corresponding to N–B, pyridinic N, pyrrolic N, and quaternary N [26]. CC@BCN@PANI showed the highest active nitrogen ratio $–N^+=$, which could bring a lower charge transfer resistance and benefit in improving the electrochemical performance [43]. The 284.3, 284.8, 285.9, and 286.7 eV in the C 1s spectrum of CC@BCN (Fig. S2(a)) demonstrated the existence of C–B, sp^2 C, C–N, and C=N bonds. Compared with the CC@PANI samples (Fig. S2(b)), CC@BCN@PANI (Fig. S2(c)) showed two new peaks at 284.3 and 288.6 eV, matched to the C–B and C–O, respectively. In addition, the C–O bonds could enhance the wettability of the CC@BCN@PANI, and promote the rate of electrode adsorption and desorption of ions in electrolytes [34]. As shown in Fig. S2(d), the B 1s spectrum of CC@BCN was deconvoluted into three peaks: 190.4, 191.3, and 192.2 eV, with the centers of B–C, B–N, and B–O bonds. The results confirmed that B was covalently bonded with C and N, which was beneficial to the chemisorption on the surface of the BCN material [44]. Furthermore, timing by electrodeposition of droplets, the CC and CC@BCN showed a contact angle of 126.1° ± 0.7° and 102.9° ± 0.3° (Fig. S3), indicating that CC@BCN has a better wettability than CC. The optimized hydrophilic properties could promote homogeneous PANI deposition in the CC@BCN electrode and reduce the ion transfer impedance in the solid-liquid interface. CC@BCN@PANI hybrid material showed more N/B synergistic active sites and a lower charge transfer resistance, which improves the charge storage capacity [26].

Typical coin-type aqueous ZHSCs were assembled based on CC@BCN, CC@PANI, and CC@BCN@PANI as cathodes. The self-discharge behavior of electrochemical energy storage devices has important implications for their practical application [45–47]. As shown in Fig. S4, the voltage of CC@BCN@PANI//Zn showed a

marked contrast with CC@BCN@PANI//CC@BCN@PANI after 100 h hole time, as it retained 78.4% of its capacity compared to a mere 16.7% capacity retention by the latter. The superior self-discharge resistance of CC@BCN@PANI//Zn was attributed to the larger voltage platform between the positive and negative terminals and a higher energy barrier for spontaneous stripping/plating associated with metal Zn in the ZHSCs compared to symmetric supercapacitors. Moreover, the CC@BCN//Zn system relies on double-layer capacitance, and the energy storage results mainly from the physical electrostatic adsorption of electrolyte ions on electrodes, leading to a faster self-discharge rate of CC@BCN//Zn. In comparison to BCN electrodes, the energy storage mechanism of PANI electrodes is based on reversible chemisorption/desorption or redox reactions. This process occurs not only on the surface of the electrode but also inside it, leading to a better anti-self-discharge performance.

The CV curves of ZHSCs were displayed in Fig. 4(a), with the voltage range from 0.1 to 1.6 V. In contrast to CC@BCN//Zn, both CC@PANI//Zn and CC@BCN@PANI//Zn exhibited distinct redox peaks on the CV curves. This was attributed to the energy storage mechanism of PANI primary through the redox reactions during charge-discharge cycling, indicating that this specific capacity was mainly provided by the pseudocapacitive behavior [48]. Notably, CC@PANI//Zn also displayed an apparent polarization at the working voltage near 0.1–0.3 V, suggesting its inferior rate performance and reversibility as the cathode of ZHSCs [49]. Moreover, CC@BCN//Zn exhibited a nearly rectangular-shaped CV curve, indicating that its capacity is mainly contributed by double-layer capacitance, which is consistent with the characteristics of carbon-based electrode

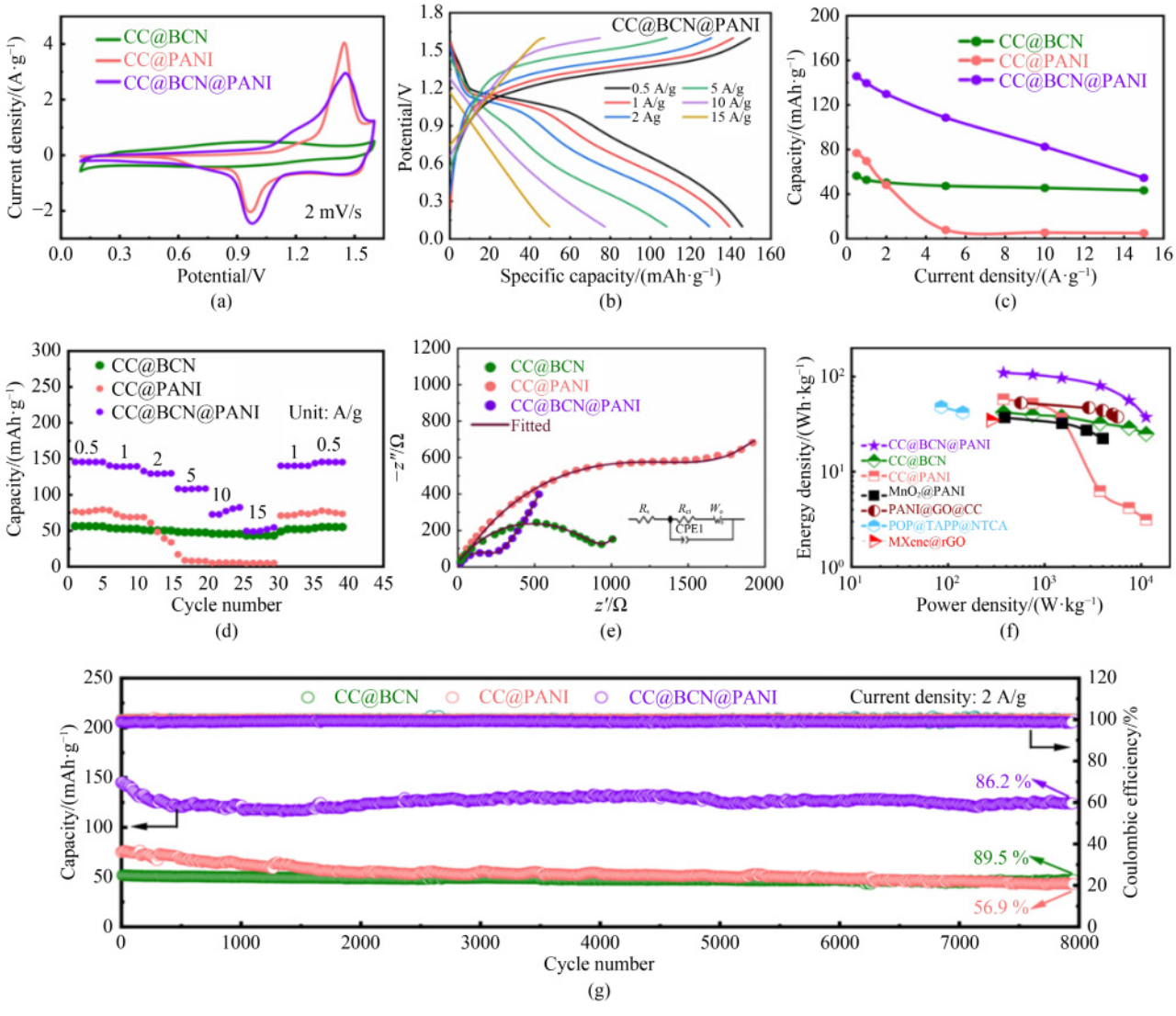

Fig. 4 Electrochemical performance of coin-type ZHSCs.

(a) CV curves at the current scan rate of 2 mV/s; (b) GCD curves at the current density from 0.5 to 15 A/g; (c) specific capacities at the current density from 0.5 to 15 A/g; (d) rate performance; (e) EIS curve and fitting results; (f) Ragone plots; (g) cycling stability at 2 A/g.

materials. Combining the advantages of both electrode materials, CC@BCN@PANI//Zn demonstrated a superior specific capacity with an excellent rate capability and cycling stability. This could be attributed to the stable electrode structure of CC@BCN@PANI and the synergistic effect of BCN component and PANI, with the electrochemical processes being jointly dominated by double-layer capacitance and pseudocapacitance. The GCD curves of the CC@BCN@PANI//Zn were displayed in Fig. 4(b), where two voltage plateaus at nearly 1.0 and 1.4 V were observed, which matched the analysis in Fig. 4(a).

The rate performance of the three cathodes materials was also evaluated in Figs. 4(c) and 4(d). CC@BCN@PANI//Zn showed a capacity of 145.8 mAh/g at 0.5 A/g, which was more than twice as many as that of CC@PANI//Zn (78.81 mAh/g) and CC@BCN//Zn (56.41 mAh/g). It was worth noting that while the current density increased to 5 A/g, the CC@BCN@PANI//Zn capacity retention rate was 73.27%, much better than the CC@PANI//Zn (10.31%). This enhanced performance could be attributed to the coordination effect of the 3D nanoarray structure and PANI of CC@BCN@PANI cathodes, as well as its stable microstructure, which could endure the expansion and contraction of PANI charge and discharge processes [50]. Specifically, the BCN 3D nanoarrays structure exhibits a stable chemical structure and abundant active sites, resulting in an increased specific surface area of the electrode and making it a suitable anchor for PANI electrochemical deposition. Additionally, its excellent conductivity facilitates the transfer of electrons along the BCN nanoarray toward PANI, promoting its involvement in the redox process and ultimately improving the electrochemical performance. The validity of this claim was further supported by the impedance spectra curves displayed in Fig. 4(e). The semicircular diameter of the high frequency region indicates the charge transfer resistance (R_{ct}) at the electrode-electrolyte interface. According to the fitting results, CC@BCN@PANI//Zn possess the smallest R_{ct} than CC@PANI//Zn and CC@BCN//Zn, which also accounted for the excellent high specific capacity and rate capability of the hybrid CC@BCN@PANI electrode. Moreover, the CC@BCN@PANI//Zn obtained a distinguished energy density of 116.78 Wh/kg, and an excellent power density of 12 kW/kg. In comparison to other reported ZHSCs, the CC@BCN@PANI cathodes exhibit a superior electrochemical performance, placing them in the forefront as depicted in Fig. 4(f) [51–54].

Cycling stability is one of the key indicators to estimate the electrochemical property of ZHSCs [55,56]. As shown in Fig. 4(g), after 8000 cycles at the current density of 2 A/g, the specific capacity of the CC@BCN@PANI//Zn remained 126.3 mAh/g (86.2%), and the Coulombic efficiency remained close to 100% during the long-term charge/discharge cycles, which implied that CC@BCN@PANI performing as the cathode of ZHSCs could have a superior electrochemical reversibility. Moreover, after undergoing approximately 1000 charge/discharge cycles, the specific capacity of CC@BCN@PANI//Zn increases. This phenomenon can be attributed to a small fraction of the the active material of the electrode, which initially fails to participate effectively in the electrochemical reaction. However, as the cycle progresses, the wettability of the material improves, allowing this fraction of the active material to gradually participate in the reaction, resulting in an increase in capacity. Overall, compared with the ZHSCs reported in the previous studies in Table S1, the CC@BCN@PANI electrode exhibits a superior performance in terms of cycling stability. The inferior cycle stability of PANI could be attributed to the expansion/contraction of the PANI molecular chain during charge/discharge cycles, as well as the sluggish electrochemical kinetics, which could causally trigger the damage to the electrode structure. The integration of BCN 3D nanoarrays and PANI could effectively enhance the active sites and ion transport rate, and improve the durability of PANI chains under expansion and contraction. Although the cycling stability of CC@BCN@PANI//Zn was slightly inferior to that of CC@BCN//Zn due to a minor shedding of PANI during the charge and discharge process, it was undoubtedly a great improvement compared to CC@PANI//Zn. Moreover, it was apparent that the 3D structure and elemental distribution of the CC@BCN@PANI cathodes were almost unchanged after 8000 charge/discharge cycles (Fig. S5). Moreover, the XRD test (Fig. S6) indicated there was little change in the position and intensity of the diffraction peak of CC@BCN@PANI, which further demonstrated the outstanding electrochemical stability of CC@BCN@PANI.

The electrochemical reaction kinetics of the CC@BCN@PANI, CC@BCN, and CC@PANI cathodes were studied based on the CV curves (Figs. 5(a), S7(a), and S8(a)). According to Eqs. (4) and (5), when the electrochemical reaction occurs, the relationship between the scanning rate v (mV/s) and the peak current i (A/g) could be applied to investigate the electrochemical performance [57].

$$i = av^b, \tag{4}$$

$$\log(i) = b\log(v) + \log a, \tag{5}$$

where a and b were variable parameters, which could be calculated by matching the plots of $\log(i)$ versus $\log(v)$. When the value of b was 0.5, the electrochemical reaction kinetics was dominated by diffusion-controlled and the response was sluggish. When the value of b was 1.0, the electrochemical reaction kinetics was controlled by the capacitive process with a quick response [58,59]. As shown in Fig. 5(b), the value of b of the oxidation and reduction peaks of CC@BCN@PANI//Zn was 0.774 and

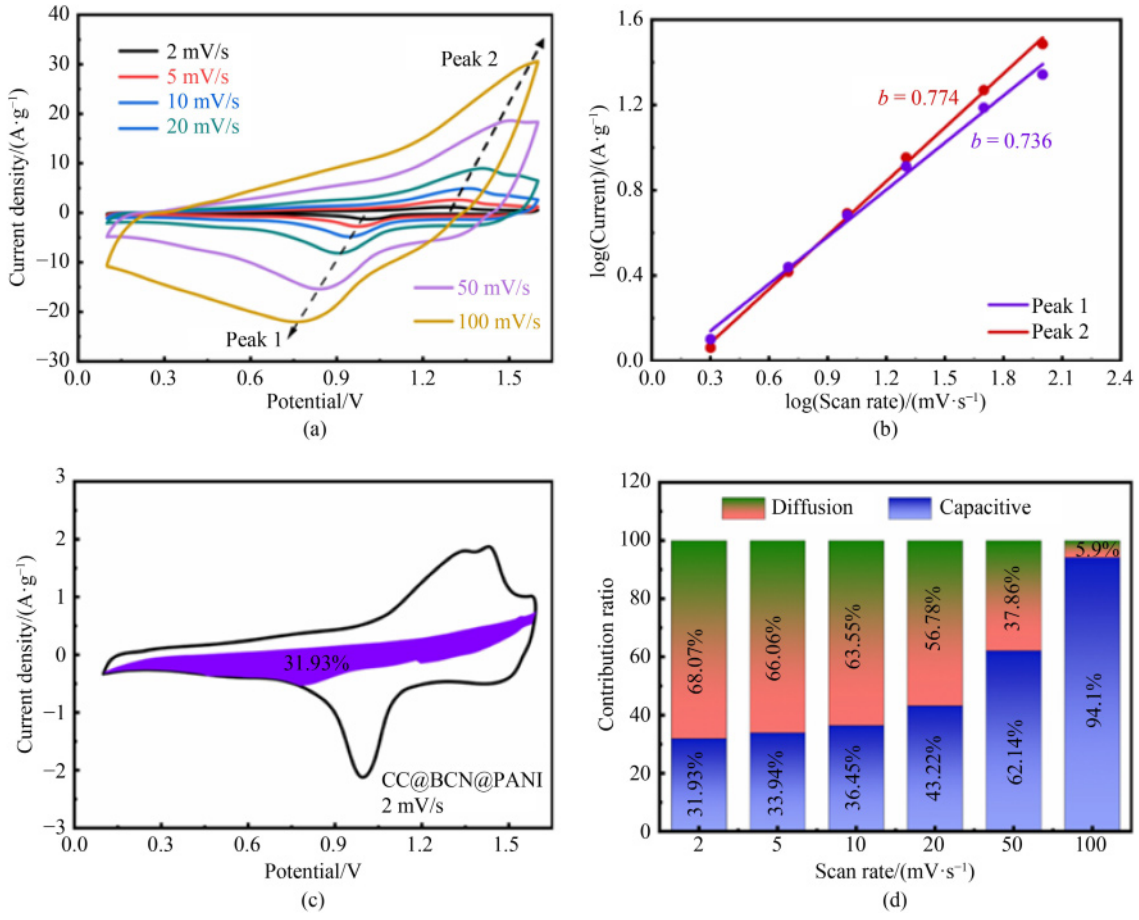

Fig. 5 Electrochemical kinetics of ZHSCs with the CC@BCN@PANI cathode.
(a) CV curves; (b) values of *b*; (c) capacitance contribution rate at 2 mV/s; (d) capacitance contribution rate at different scan rates.

0.736, while the CC@PANI//Zn corresponded to 0.697 (Fig. S8(b)). Moreover, the values of *b* of the CC@BCN//Zn were 0.83 (anodic peak current) and 0.819 (cathodic peak current) (Fig. S7(b)). All three types of CC cathodes were between 0.5 and 1.0, indicating that the electrochemical reaction processes of CC@BCN, CC@PANI, and CC@BCN@PANI-based ZHSCs were synergistically controlled by capacitive and diffusion behaviors. Hence, according to Eq. (6), the current generated in an electrochemical reaction can be grouped into two parts [60]:

$$i = k_1 v + k_2 v^{\frac{1}{2}}. \tag{6}$$

Furthermore, to evaluate the response current contribution quantitatively, $k_1 v$ represents the capacitance effect and $k_2 v^{1/2}$ represents diffusion behaviors [61]. As displayed in Fig. 5(c), almost 31.93% of the capacity was contributed by the capacitive process for the CC@BCN@PANI//Zn at 2 mV/s (violet area). The capacitive contribution ratio increased from 31.93% to 94.1%, when the current scanning rate increased from 2 to 100 mV/s, whereas the diffusion contribution ratio decreased from 68.07% to 5.9% (Fig. 5(d)). For CC@BCN and CC@PANI based ZHSCs, the capacitive process contributed from 73.3% to 99.12% (Fig. S7(d)) and 26.8% to 92.52% (Fig. S8(d)). Since the capacitive process has quick kinetics, it is easier for the CC@BCN@PANI cathodes to achieve a rapid charge/discharge than the CC@PANI cathodes, which were consistent with the rate capability and EIS results analyzed in Figs. 4(d) and 4(e).

Based on the above analysis, the energy storage mechanism of the ZHSCs with the CC@BCN@PANI cathode could be concluded as follows: During charge/discharge cycles, Zn anodes experienced a reversible plating/stripping. The CC@BCN@PANI nanocomposite cathode stored/released energy by the capacitive mechanism and the redox process [62–64]. More specifically, the energy storage of the PANI component was mainly attributed to the Faraday redox reaction which facilitated the transfer of charges, whereas the CC@BCN component stored energy mainly through ion adsorption/desorption (i.e., double-layer capacitor). The synergistic coordination mechanism between the PANI and CC@BCN components resulted in outstanding electrochemical properties of the CC@BCN@PANI composite.

The high safety and excellent electrochemical perfor-

mance of aqueous ZHSCs with the CC@BCN@PANI cathodes also could be used for FZHSCs. The structure of FZHSCs was shown in Fig. 6(a), with CC@BCN@PANI composites as the cathode, Zn foil as the anode, GGE as the gel electrolyte and diaphragm, and polyimide tape used to encapsulate the FZHSCs, respectively. As shown in Fig. 6(b), the FZHSCs had an outstanding discharge capacity of 160 mAh/g at the current density of 0.1 A/g, and 93.29 mAh/g at 0.5 A/g. As shown in Fig. 6(c), to test the flexible performance of CC@BCN@PANI-based FZHSCs, the devices could be bent from 0° to 180° and still maintained a nearly constant discharge capacity at the current density of 0.5 A/g. Additionally, the capacity retention of FZHSCs after 200 cycles of 90° bending at a current density of 2 A/g was simultaneously studied. As revealed in Fig. S9, the capacity retention reached 86.2% after repeated bending, which verified the best performance of the prepared FZHSCs in terms of the excellent flexibility. Notably, the specific capacity of the device increased slightly after 80 bending cycles, which could be attributed to the slight increase in temperature during the bending process (i.e., frictional heating), leading to an improved ion conductivity of the gel electrolyte [65]. The excellent electrochemical performance and remarkable flexibility are due to the fact that the CC@BCN@PANI 3D nanoarray structure can relieve the stress produced by the twisting of the electrodes, avoid cracking and shedding of the active material, and keep the electrode structure stable. Moreover, when two FZHSCs were connected to light an LED, it could maintain a high brightness after 30 min of continuous working (Fig. 6(d)), demonstrating the stability and excellent energy output of the FZHSCs devices. Furthermore, the capacity retention rate reached 87.7% at the current density of 2 A/g after 450 cycles (Fig. 6(e)). It should be noted that compared to coin-type ZHSCs, the specific capacity of CC@BCN@PANI-based FZHSCs decreases significantly. This is attributed to the fact that the gel electrolyte used in FZHSCs have a lower ion conductivity and a higher interfacial transfer resistance than the $ZnSO_4$ aqueous electrolyte used in coin-type ZHSCs.

The modification and optimization of Zn anodes were widely considered crucial elements in producing FZHSCs with a superior electrochemical performance. However, it should be noted that in the experiments, Zn foils served as direct substitutes for Zn anodes. While employing Zn foil for anode fabrication of FZHSCs could simplify assembly, it also constrains the capacity for further enhancement of the FZHSCs performance. Moreover, electrochemical reactions may induce secondary reactions alongside the Zn foil, resulting in Zn passivation and Zn dendrite formation, thereby significantly impacting the cycle life of FZHSCs, suggesting that the utilization of Zn foil for anode preparation was not ideal [6,66]. Therefore, future research will focus on discovering solution strategies, such as minimizing the occurrence of Zn dendrites and mitigating the negative effects of secondary reactions on electrode performance.

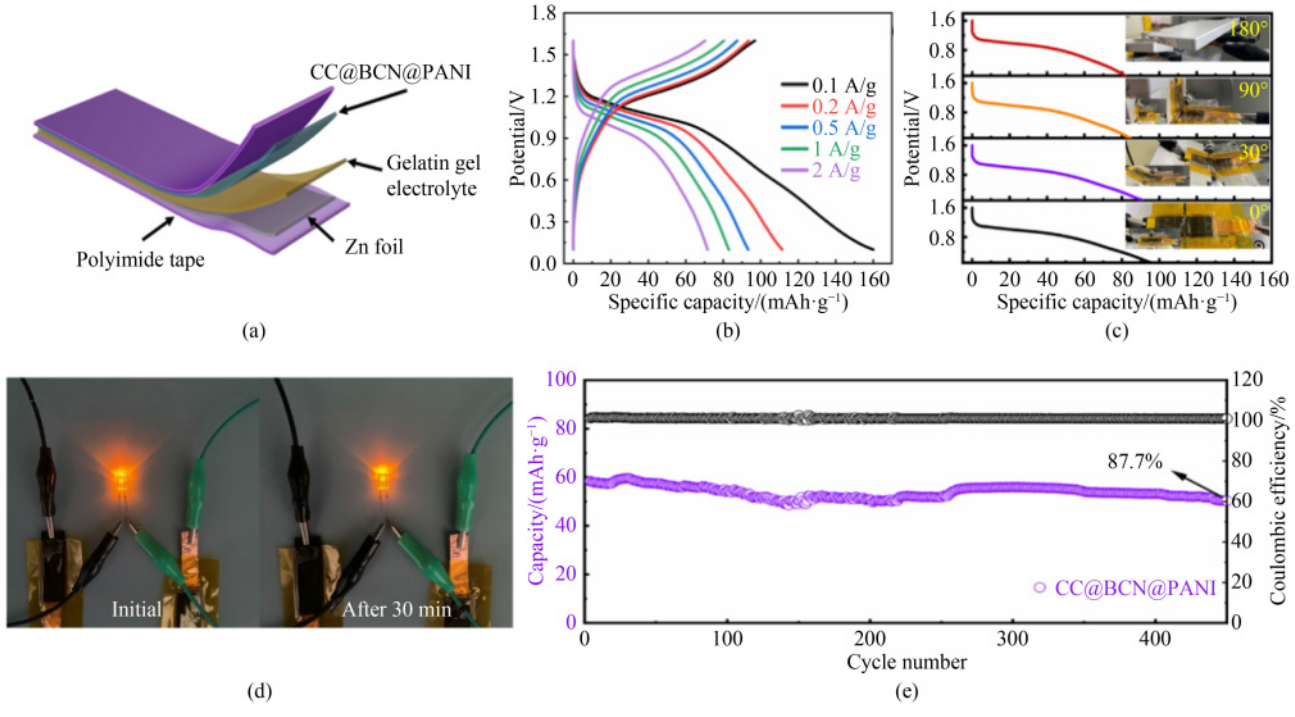

Fig. 6 Physical capabilities and electrical behavior of FZHSCs.

(a) Structure of FZHSCs; (b) GCD curves; (c) discharge curves at various bending angles at the current density of 0.5 A/g; (d) LED powered by the devices; (e) cycling stability at the current density of 2 A/g.

To achieve this, a Zn anode with a 3D composite structure will be developed, as it offers exceptional flexibility and promotes the homogenous deposition of Zn^{2+} onto the anode.

4 Conclusions

In general, high-performance and flexible ZHSCs using functionalized CC@BCN@PANI cathodes were designed. The ZHSCs showed an outstanding electrochemical performance, such as a high specific capacitance of 145.8 mAh/(0.5 A/g), a high energy density of 116.78 Wh/kg, a high power density of 12 kW/kg, and an ultra-high cycle life with a capacity retention rate of 86.2% after 8000 cycles. Further, the FZHSCs devices assembled with CC@BCN@PANI electrodes as positive electrodes also exhibit an excellent energy output, an excellent bending performance, and an excellent stability. This research has provided a reference for the design of conductive polymer and 3D carbon nanoarrays hybrid electrodes for high performance FZHSCs.

Acknowledgements This work was supported by the Natural Science Foundation of Jiangxi Province (Grant Nos. 20224BAB214006, 20224BAB214029, and 20212ACB203004), the Planning Project of Jiangxi Provincial Technological Innovation Guidance (Grant No. 20202BDH80003), and the Youth Foundation of Jiangxi Provincial Department of Education (Grant Nos. GJJ210857 and GJJ210856).

Competing interests The authors declare that they have no competing interests.

Electronic Supplementary Material Supplementary material is available in the online version of this article at https://doi.org/10.1007/s11708-023-0882-8 and is accessible for authorized users.

References

1. Wang R, Yao M, Niu Z. Smart supercapacitors from materials to devices. InfoMat, 2020, 2(1): 113–125
2. Fu Q, Hao S, Zhang X, et al. All-round supramolecular zwitterionic hydrogel electrolytes enabling environmentally adaptive dendrite-free aqueous zinc ion capacitors. Energy & Environmental Science, 2023, 16(3): 1291–1311
3. Ock I W, Lee J, Kang J K. Metal-organic framework-derived anode and polyaniline chain networked cathode with mesoporous and conductive pathways for high energy density, ultrafast rechargeable, and long-life hybrid capacitors. Advanced Energy Materials, 2020, 10(48): 2001851
4. Mennel J A, Chidambaram D. A review on the development of electrolytes for lithium-based batteries for low temperature applications. Frontiers in Energy, 2023, 17(1): 43–71
5. Jiang D, Li C, Yang W, et al. Fabrication of an arbitrary-shaped and nitrogen-doped graphene aerogel for highly compressible all solid-state supercapacitors. Journal of Materials Chemistry. A, Materials for Energy and Sustainability, 2017, 5(35): 18684–18690
6. Tang H, Yao J J, Zhu Y. Recent developments and future prospects for zinc-ion hybrid capacitors: A review. Advanced Energy Materials, 2021, 11(14): 2003994
7. Xie C, Li Y, Wang Q, et al. Issues and solutions toward zinc anode in aqueous zinc-ion batteries: A mini review. Carbon Energy, 2020, 2(4): 540–560
8. Hu C, Wu A, Zhu F, et al. Lithium-ion modified cellulose as a water-soluble binder for Li-O_2 battery. Frontiers in Energy, 2022, 16(3): 502–508
9. Choudhary N, Li C, Moore J L, et al. Asymmetric supercapacitor electrodes and devices. Advanced Materials, 2017, 29(21): 1605336
10. Zou K, Cai P, Liu C, et al. A kinetically well-matched full-carbon sodium-ion capacitor. Journal of Materials Chemistry. A, Materials for Energy and Sustainability, 2019, 7(22): 13540–13549
11. Chen J, Yang B, Hou H, et al. Disordered, large interlayer spacing, and oxygen-rich carbon nanosheets for potassium ion hybrid capacitor. Advanced Energy Materials, 2019, 9(19): 1803894
12. Han P, Xu G, Han X, et al. Lithium-ion capacitors in organic electrolyte system: Scientific problems, material development, and key technologies. Advanced Energy Materials, 2018, 8(26): 1801243
13. Wu N, Yao W, Song X, et al. A calcium-ion hybrid energy storage device with high capacity and long cycling life under room temperature. Advanced Energy Materials, 2019, 9(16): 1803865
14. Ma X, Cheng J, Dong L, et al. Multivalent ion storage towards high-performance aqueous zinc-ion hybrid supercapacitors. Energy Storage Materials, 2019, 20(46): 335–342
15. Dubey R J, Colijn T, Aebli M, et al. Zeolite-templated carbon as a stable, high power magnesium-ion cathode material. ACS Applied Materials & Interfaces, 2019, 11(43): 39902–39909
16. Song M, Tan H, Chao D, et al. Recent advances in Zn-ion batteries. Advanced Functional Materials, 2018, 28(41): 1802564
17. Su L, Liu L, Liu B, et al. Revealing the impact of oxygen dissolved in electrolytes on aqueous zinc-ion batteries. iScience, 2020, 23(4): 100995
18. Tang B, Shan L, Liang S, et al. Issues and opportunities facing aqueous zinc-ion batteries. Energy & Environmental Science, 2019, 12(11): 3288–3304
19. Han L, Huang H, Fu X, et al. A flexible, high-voltage and safe zwitterionic natural polymer hydrogel electrolyte for high-energy-density zinc-ion hybrid supercapacitor. Chemical Engineering Journal, 2020, 392: 123733
20. Pu J, Cao Q, Gao Y, et al. Ultrafast-charging quasi-solid-state fiber-shaped zinc-ion hybrid super-capacitors with superior flexibility. Journal of Materials Chemistry. A, Materials for Energy and Sustainability, 2021, 9(32): 17292–17299
21. Xu X, Tang J, Qian H, et al. Three-dimensional networked metal-organic frameworks with conductive polypyrrole tubes for flexible supercapacitors. ACS Applied Materials & Interfaces, 2017, 9(44): 38737–38744

22. Wang Y, Jiang H, Zheng R, et al. A flexible, electrochromic, rechargeable Zn-ion battery based on actiniae-like self-doped polyaniline cathode. Journal of Materials Chemistry. A, Materials for Energy and Sustainability, 2020, 8(25): 12799–12809
23. Borges J, Rodrigues L C, Reis R L, et al. Layer-by-layer assembly of light-responsive polymeric multilayer systems. Advanced Functional Materials, 2014, 24(36): 5624–5648
24. Hu L, Wan Y, Zhang Q, et al. Harnessing the power of stimuli-responsive polymers for actuation. Advanced Functional Materials, 2020, 30(2): 1903471
25. Li C, Zheng C, Cao F, et al. The development trend of graphene derivatives. Journal of Electronic Materials, 2022, 51(8): 4107–4114
26. Liang Z, Tu H, Shi D, et al. *In-situ* growing BCN nanotubes on carbon fibers for novel high-temperature supercapacitor with excellent cycling performance. Small, 2021, 17(51): 2102899
27. Wang X, Feng Z, Hou X, et al. Fluorine doped carbon coating of $LiFePO_4$ as a cathode material for lithium-ion batteries. Chemical Engineering Journal, 2020, 379(56): 122371
28. Xu Y, Jiang J, Li Z, et al. Aerosol-assisted preparation of N-doped hierarchical porous carbon spheres cathodes toward high-stable lithium-ion capacitors. Journal of Materials Science, 2020, 55(27): 13127–13140
29. Yang J, Zhai Y, Zhang X, et al. Perspective on carbon anode materials for K^+ storage: Balancing the intercalation-controlled and surface-driven behavior. Advanced Energy Materials, 2021, 11(29): 2100856
30. Tabassum H, Zou R, Mahmood A, et al. A universal strategy for hollow metal oxide nanoparticles encapsulated into B/N co-doped graphitic nanotubes as high-performance lithium-ion battery anodes. Advanced Materials, 2018, 30(8): 1705441
31. Tabassum H, Guo W, Meng W, et al. Metal-organic frameworks derived cobalt phosphide architecture encapsulated into B/N Co-doped graphene nanotubes for all pH value electrochemical hydrogen evolution. Advanced Energy Materials, 2017, 7(9): 1601671
32. Tabassum H, Qu C, Cai K, et al. Large-scale fabrication of BCN nanotube architecture entangled on a three-dimensional carbon skeleton for energy storage. Journal of Materials Chemistry. A, Materials for Energy and Sustainability, 2020, 8(25): 21225–21230
33. Fu N, Liu Y, Liu R, et al. Metal cation-assisted synthesis of amorphous B, N co-doped carbon nanotubes for superior sodium storage. Small, 2020, 16(20): 2001607
34. Shi L, Ye J, Lu H, et al. Flexible all-solid-state supercapacitors based on boron and nitrogen-doped carbon network anchored on carbon fiber cloth. Chemical Engineering Journal, 2021, 410(55): 128365
35. Cong Z, Guo W, Zhang P, et al. Wearable antifreezing fiber-shaped Zn/PANI batteries with suppressed Zn dendrites and operation in sweat electrolytes. ACS Applied Materials & Interfaces, 2021, 13(15): 17608–17617
36. Cao L, Wang Y, Zhu Q, et al. Co/Co−N/Co−O rooted on rGO hybrid BCN nanotube arrays as efficient oxygen electrocatalyst for Zn-air batteries. ACS Applied Materials & Interfaces, 2022, 14(15): 17249–17258
37. Wang S, Ma F, Jiang H, et al. Band gap-tunable porous borocarbonitride nanosheets for high energy-density supercapacitors. ACS Applied Materials & Interfaces, 2018, 10(23): 19588–19597
38. Yang M, Shi D, Sun X, et al. Shuttle confinement of lithium polysulfides in borocarbonitride nanotubes with enhanced performance for lithium-sulfur batteries. Journal of Materials Chemistry. A, Materials for Energy and Sustainability, 2020, 8(1): 296–304
39. Gu D, Ding C, Qin Y, et al. Behavior of electrical charge storage/release in polyaniline electrodes of symmetric supercapacitor. Electrochimica Acta, 2017, 245(17): 146–155
40. Li X, Li Y, Xie S, et al. Zinc-based energy storage with functionalized carbon nanotube/polyaniline nanocomposite cathodes. Chemical Engineering Journal, 2022, 427(59): 131799
41. Cao L, Zhou X, Li Z, et al. Nitrogen and fluorine hybridization state tuning in hierarchical honeycomb-like carbon nanofibers for optimized electrocatalytic ORR in alkaline and acidic electrolytes. Journal of Power Sources, 2019, 413(15): 376–383
42. Liao X, Pan C, Yan H, et al. Polyaniline-functionalized graphene composite cathode with enhanced Zn^{2+} storage performance for aqueous zinc-ion battery. Chemical Engineering Journal, 2022, 440(18): 135930
43. Li W, Gao F, Wang X, et al. Strong and robust polyaniline-based supramolecular hydrogels for flexible supercapacitors. Angewandte Chemie, 2016, 128(32): 9342–9347
44. Wang D W, Li F, Chen Z G, et al. Synthesis and electrochemical property of boron-doped mesoporous carbon in supercapacitor. Chemistry of Materials, 2008, 20(22): 7195–7200
45. Huang Z, Wang T, Song H, et al. Effects of anion carriers on capacitance and self-discharge behaviors of zinc ion capacitors. Angewandte Chemie, 2021, 133(2): 1024–1034
46. Yang J, Bissett M A, Dryfe R A W. Investigation of coltage range and self-discharge in aqueous zinc-ion hybrid supercapacitors. ChemSusChem, 2021, 14(7): 1700–1709
47. Huang Z, Chen A, Mo F, et al. Phosphorene as cathode material for high-voltage, anti-self-discharge zinc ion hybrid capacitors. Advanced Energy Materials, 2020, 10(24): 2001024
48. Song T, Hao H, Zhao Y, et al. High-performance Zn-ion hybrid supercapacitor enabled by the hierarchical N/S co-doped graphene/polyaniline cathode. Journal of Alloys and Compounds, 2022, 924: 166493
49. Ruan P, Xu X, Gao X, et al. Achieving long-cycle-life Zn-ion batteries through interfacial engineering of MnO_2-polyaniline hybrid networks. Sustainable Materials and Technologies, 2021, 28: e00254
50. Luo Y, Guo R, Li T, et al. Application of polyaniline for Li-ion batteries, lithium-sulfur batteries, and supercapacitors. ChemSusChem, 2019, 12(8): 1591–1611
51. Ghosh K, Yue C Y, Sk M M, et al. Development of 3D urchin-shaped coaxial manganese dioxide@polyaniline (MnO_2@PANI) composite and self-assembled 3D pillared graphene foam for asymmetric all-solid-state flexible supercapacitor application. ACS Applied Materials & Interfaces, 2017, 9(18): 15350–15363
52. Shen Y, Qin Z, Hu S Y, et al. *In-situ* hybridization of graphene sheets onto polyaniline nanofiber arrays grown on the surface of

carbon cloth under high electric voltage field for high-performance flexible supercapacitor. Carbon, 2020, 158(14): 711–718

53. Cui F Z, Liu Z, Ma D L, et al. Polyarylimide and porphyrin-based polymer microspheres for zinc ion hybrid capacitors. Chemical Engineering Journal, 2021, 405(26): 127038
54. Wang Q, Wang S, Guo X, et al. MXene-reduced graphene oxide aerogel for aqueous zinc-ion hybrid supercapacitor with ultralong cycle life. Advanced Electronic Materials, 2019, 5(12): 1900537
55. Huang Z, Zhang R, Zhang S, et al. Recent advances and future perspectives for aqueous zinc-ion capacitors. Materials Futures, 2022, 1(2): 022101
56. Liang G, Li X, Wang Y, et al. Building durable aqueous K-ion capacitors based on MXene family. Nano Research Energy, 2022, 1(1): e9120002
57. Xu L, Pan G, Yu C, et al. Co-doped MnO_2 with abundant oxygen vacancies as a cathode for superior aqueous magnesium ion storage. Inorganic Chemistry Frontiers, 2023, 10(6): 1748–1757
58. Li Y, Yang W, Huang Y, et al. High-performance zinc-ion batteries enabled by electrochemically induced trans-formation of vanadium oxide cathodes. Journal of Energy Chemistry, 2021, 60(17): 233–240
59. Luo P, Xiao Y, Yang J, et al. Polyaniline nanoarrays/carbon cloth as binder-free and flexible cathode for magnesium ion batteries. Chemical Engineering Journal, 2022, 433(14): 133772
60. Chen L, Xu X, Wan L, et al. Carbon-incorporated Fe_3O_4 nanoflakes: High-performance faradaic materials for hybrid capacitive deionization and supercapacitors. Materials Chemistry Frontiers, 2021, 5(8): 3480–3488
61. Lu Y, Li Z, Bai Z, et al. High energy-power Zn-ion hybrid supercapacitors enabled by layered B/N co-doped carbon cathode. Nano Energy, 2019, 66(17): 104132
62. Dong L, Ma X, Li Y, et al. Extremely safe, high-rate and ultralong-life zinc-ion hybrid super-capacitors. Energy Storage Materials, 2018, 13(56): 96–102
63. Han J, Wang K, Liu W, et al. Rational design of nano-architecture composite hydrogel electrode towards high performance Zn-ion hybrid cell. Nanoscale, 2018, 10(27): 13083–13091
64. Yao M, Yuan Z, Li S, et al. Scalable assembly of flexible ultrathin all-in-one zinc-ion batteries with highly stretchable, editable, and customizable functions. Advanced Materials, 2021, 33(10): 2008140
65. Chen L, Fu J, Lu Q, et al. Cross-linked polymeric ionic liquids ion gel electrolytes by *in situ* radical polymerization. Chemical Engineering Journal, 2019, 378: 122245
66. Dong L, Yang W, Yang W, et al. Multivalent metal ion hybrid capacitors: A review with a focus on zinc-ion hybrid capacitors. Journal of Materials Chemistry. A, Materials for Energy and Sustainability, 2019, 7(23): 13810–13832